

Internal Diffusion-Controlled Enzyme Reaction: The Acetylcholinesterase Kinetics

Sangyun Lee, Ji-Hyun Kim, and Sangyoub Lee*

Department of Chemistry, Seoul National University, Seoul 151-747, S. Korea

S Supporting Information

ABSTRACT: Acetylcholinesterase is an enzyme with a very high turnover rate; it quenches the neurotransmitter, acetylcholine, at the synapse. We have investigated the kinetics of the enzyme reaction by calculating the diffusion rate of the substrate molecule along an active site channel inside the enzyme from atomic-level molecular dynamics simulations. In contrast to the previous works, we have found that the internal substrate diffusion is the determinant of the acetylcholinesterase kinetics in the low substrate concentration limit. Our estimate of the overall bimolecular reaction rate constant for the enzyme is in good agreement with the experimental data. In addition, the present calculation provides a reasonable explanation for the effects of the ionic strength of solution and the mutation of surface residues of the enzyme. The study suggests that internal diffusion of the substrate could be a key factor in understanding the kinetics of enzymes of similar characteristics.

INTRODUCTION

Acetylcholinesterase (AChE, EC 3.1.1.7) is an enzyme working at the neuronal synapse to quench the chemical signal transmitter, acetylcholine (ACh), which is released from the presynaptic nerve terminal in response to an external electrical impulse, called an action potential.¹ AChE has evolved into one of the fastest enzymes because ACh must be degraded rapidly to restore the synapse to the initial phase for receiving the next neural signal transmission. The structure and function of AChE have been studied for many years by both experimental and computational approaches because of AChE's importance in neural signal transmission; it is also a target enzyme for the treatment of Alzheimer's disease.²

The active site of the enzyme involves O[−] of Ser203 (in mouse AChE), which catalyzes the hydrolysis reaction of ACh via nucleophilic attack on the carbonyl C of ACh.¹ An interesting feature of the enzyme structure is that the active site is located at the bottom of a narrow channel that is about 20 Å long (see Figure 1).³ Nevertheless, the enzyme reaction rate is very fast, approaching the diffusion-controlled regime.^{4–8}

McCammon and co-workers calculated the rate of approach of the substrate molecule from the bulk to the entrance of the active site channel by using the Brownian dynamics (BD) simulation method,^{9–11} but the calculated rate was about 2 orders of magnitude larger than the observed enzyme reaction rate. Subsequently, they investigated the rate of diffusive motion of the substrate molecule along the active site channel by molecular dynamics (MD) simulation but found that the time required for the substrate passing through the channel was not a determinant of the reaction kinetics, at least for the AChE–ACh reaction, although this internal diffusion step influences significantly the kinetics of some mutant enzymes and inhibitors.¹²

However, the observed dependence of the bimolecular enzyme–substrate reaction rate on the viscosity and the ionic strength of solution indicates that the enzyme reaction is not fully activation-controlled.^{5,6} That is, the time spent for the substrate molecule to reach the buried active site must be comparable to the overall reaction time. In this work, we have evaluated the rate of diffusive

motion of the substrate molecule inside the active site channel from full-atom MD simulations. In contrast to the previous computational studies, we find that the internal diffusion of the substrate molecule along the active site channel is the determinant of the AChE–ACh kinetics. In the low substrate concentration limit, the movement of the substrate molecule from the channel entrance to the active site is the rate-determining step.

Experimental investigations of the AChE kinetics have been carried out using acetylthiocholine (ATCh), instead of ACh, as the substrate. In ATCh, the carboxyl group (–COO[−]) in ACh is replaced by the –COS– group. The kinetic data for the AChE–ATCh reaction are similar to those for the AChE–ACh reaction but can be measured more accurately by observing the change of the concentration of one of the products, thiocholine.⁴ Experimental values of the apparent bimolecular rate constant k_{app} vary with the viscosity, η , and the ionic strength, I , of the solution. In 100 mM phosphate buffer at pH 7.0 and 22 °C, for which $I = 179$ mM, $k_{app} = 5.0 \times 10^7$ M^{−1} s^{−1} and 5.2×10^7 M^{−1} s^{−1} for mouse AChE (mAChE)¹³ and *Torpedo californica* AChE (TcAChE),⁷ respectively.

In this work, we will present the result of calculations on the mAChE–ATCh reaction system at 22 °C and 179 mM ionic strength. Our theoretical estimate of k_{app} is 6.4×10^7 M^{−1} s^{−1}, which is in good agreement with the experimental result, considering the complexity of the reaction system. In addition, it will be seen that our refined mechanistic picture provides reasonable explanations for the effects of the ionic strength of solution and the enzyme mutation on the overall reaction rate.

THEORY AND MODELING DETAILS

Kinetics in the Low Substrate Concentration Regime.

For the purpose of calculation, we may divide the reaction pathway into three steps: (1) the approach of the substrate molecule from bulk to the active site channel entrance, (2)

Received: September 23, 2011

Published: January 18, 2012

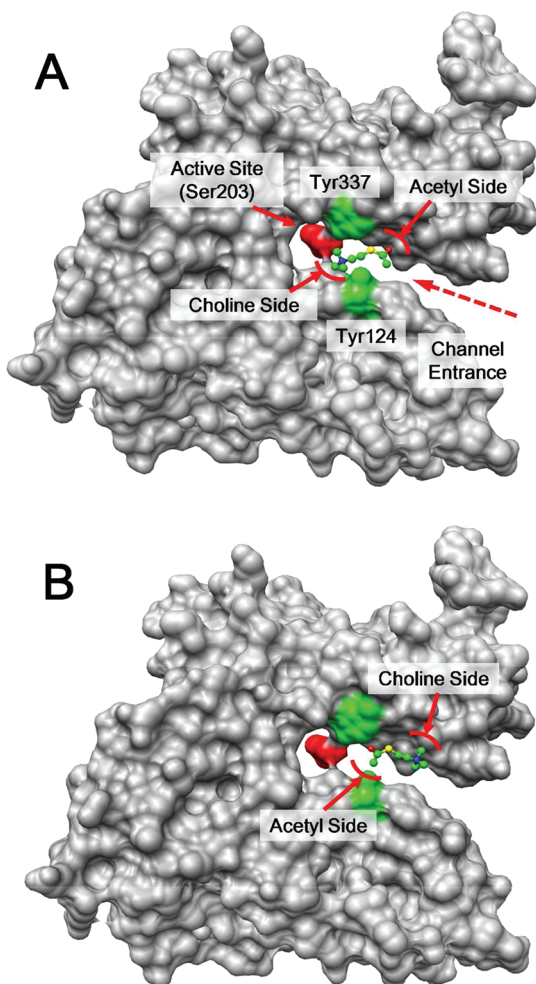


Figure 1. van der Waals surface of AChE, cross-sectioned along the active-site channel axis. The active site (Ser203, red) of the enzyme is colored red, and the bottleneck region of the channel between Tyr337 and Tyr124 is colored green. The substrate molecule is represented by a ball-and-stick model with the C, N, O, and S atoms colored green, blue, red, and yellow, respectively; hydrogen atoms are not depicted.

the hindered movement of the substrate molecule along the channel to the active site, and (3) the reactive transition at the active site.

Preliminary MD simulations show that the substrate molecule cannot rotate at the narrow part of the channel, although there is a roomier space close to the active site where it can change its orientation to form a proper enzyme–substrate (ES) complex. Therefore, we have to consider two modes of substrate movement along the channel; it may approach the active site with either the choline or acetyl part at the front side (see Figure 1).

The reaction pathways under consideration are depicted in Scheme 1, where E, S, and P denote enzyme, substrate, and

product, respectively. E–S and E–S' denote the states in which the substrate molecule anchors at the channel entrance with the choline part and with the acetyl part oriented toward the active site, respectively. The various k values refer to the rate constants for the respective steps.

Applying the steady-state approximation, we can obtain the following rate equation in the low substrate concentration limit:

$$\text{rate} = \frac{k_D}{1 + (k_{-D}/k_3)}[E][S] \quad (1)$$

where k_D and k_{-D} are the overall rate constants for the formation and dissociation of the ES complex that are respectively given by

$$k_D = \frac{k_1 k_2}{k_{-1} + k_2} + \frac{k'_1 k'_2}{k'_{-1} + k'_2};$$

$$k_{-D} = \frac{k_{-1} k_{-2}}{k_{-1} + k_2} + \frac{k'_{-1} k'_{-2}}{k'_{-1} + k'_2} \quad (2)$$

The fact that the apparent bimolecular rate constant, $k_{\text{app}} = k_D/[1 + (k_{-D}/k_3)]$, is influenced by diffusion indicates that k_3 should be large enough and has at least a comparable magnitude with k_{-D} . If $k_3 \gg k_{-D}$, we will have $k_{\text{app}} \cong k_D$, which is the diffusion-controlled limit.

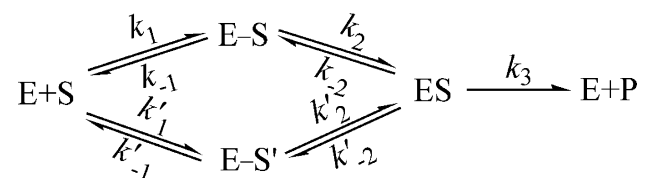
In the present work, we calculate the rate constants k_2 and k'_2 for the internal diffusion step in Scheme 1 based on full-atom MD simulations of mAChE–ATCh reaction system. The rate constants k_1 and k'_1 for the external diffusion step may be estimated by BD simulation methods. We will use the BD results of Antosiewicz et al.,⁹ who obtained $k_1 = 1.03 \times 10^9 \text{ M}^{-1} \text{ s}^{-1}$ and $k'_1 = 0.67 \times 10^9 \text{ M}^{-1} \text{ s}^{-1}$ for TcAChE and ACh, modeled as a charged dumbbell, at 300 K, pH 7, and 150 mM ionic strength; see the results given in Table 1 of ref 9 for ligand models C and D with a 3 Å reaction zone. Although there are some differences between our MD simulation model and the BD model of Antosiewicz et al., they will not change our final estimates much for k_D because what we actually need are the orders of magnitude of k_1 and k'_1 , as will be explained below. In fact, considering that the external and internal electrostatic potentials of mAChE and TcAChE as well as their structures are very similar,¹⁴ the values of k_1 and k'_1 for mAChE would not be much different from those for TcAChE.

k_2 and k'_2 can be equated to the inverse of the mean first passage time (MFPT) of the substrate from the channel entrance region to the active site.¹⁵ To calculate the MFPT, we need the potential of mean force (PMF) and the position-dependent diffusion coefficient of the substrate molecule along the channel. For simplicity, we consider the one-dimensional motion of the substrate molecule along the channel axis. Although the distance between O' of Ser203 and carbonyl C of ATCh may be appropriately defined as the reaction coordinate, the positional fluctuations of these atoms are quite large. Fortunately, residue Ser203 is located very close to the center of mass (CM) of the enzyme. We therefore define the reaction coordinate ζ as the distance between the CMs of the whole enzyme and the ATCh molecule. When ζ gets close to 8.5 Å, the distance between O' of Ser203 and carbonyl C of ATCh becomes less than 4.5 Å.

Details of MD Simulations. MD simulations of the AChE–ATCh reaction system have been carried out using CHARMM (version c34b1)¹⁶ with the all-atom parameter set 22¹⁷ and a constant relative permittivity ($\epsilon_r = 1$).

The structure of mouse AChE was taken from the Protein Data Bank (PDB code 1KU6).¹⁸ After removing the inhibitor FAS-II, the missing residues 259–262 were reconstructed using the standard parameters for the internal coordinates. The other missing residues,

Scheme 1. Reaction Scheme in the Low Substrate Concentration Regime



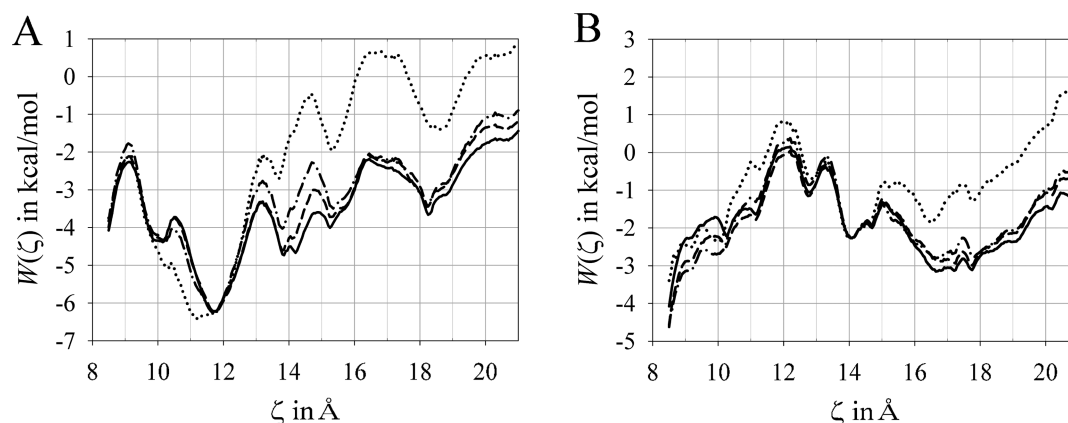


Figure 2. Convergence of the PMF profiles with respect to the time length of MD trajectories: 0.25 ns (dotted curve), 0.50 ns (dot-dashed curve), 0.75 ns (dashed curve), and 1.0 ns (solid curve). Part A shows the variation of PMF when ATCh moves toward the active site with the choline part at the front side, while part B shows the variation when the acetyl part is on the front side.

1–2 and 542–549, do not affect the reaction dynamics and were not included. Three disulfide bridges were added between the following pairs of residues: Cys67–Cys94, Cys255–Cys270, and Cys407–Cys527. Hydrogen atoms were added using the HBUILD routine of CHARMM.¹⁹ The protonation site of each histidine residue was determined on the basis of the availability of a hydrogen bond donor or acceptor near the N^δ and N^ε atoms of histidine. In the absence of available hydrogen bonds, we assumed the N^δ-protonated form. The histidine residues at positions 284, 287, 387, 393, 405, and 447 were taken to be the N^δ-protonated forms, while those at positions 381 and 432 were the N^ε-protonated forms.

For the ATCh molecule, the atomic partial charges were determined from *ab initio* calculation at the HF/6-31G* level by using the GAMESS program,²⁰ and the other potential parameters were taken from the CHARMM parameter file. To place the ATCh molecule at a chosen location in the active site channel, we took the following procedure. First, the configuration of the ATCh molecule in the active site (ES state) was determined on the basis of the crystal structure of the AChE–ACh complex (PDB code 2ACE).²¹ Then, the substrate was pulled out to the desired location by imposing additional harmonic potentials successively at 0.25 Å intervals along the reaction coordinate.

The whole AChE–ATCh structure was then placed at the center of a rhombic dodecahedron box of volume 551 nm³ and solvated with TIP3P water molecules. The CHARMM parameter designating the simulation box size was 92 Å, which is the length of the long diagonal of each rhombic face. The numbers of water molecules inside and outside of the enzyme varied slightly, depending on the location of the substrate molecule inside the enzyme. About 16 950 water molecules were included.

To simulate the experimental condition under which the AChE kinetics were studied, we then added ions to make a 179 mM ionic strength solution. Since the number density of water molecules is 0.033 Å⁻³, the solvent volume can be calculated from the number of the water molecules. Considering the solvent volume and the charge neutrality of the system, 48 sodium ions and 41 chloride ions were added outside the enzyme.

As mentioned above, the reaction coordinate ζ was defined as the distance between the CMs of the whole enzyme and the ATCh molecule. Because of the steric restraints on the ATCh molecule, ζ follows the axis of the active site channel. We used the umbrella sampling technique to calculate the PMF profile, $W(\zeta)$, and the position-dependent diffusion coefficient, $D(\zeta)$. We set up 49 sampling windows along the reaction coordinate

from 9 Å to 21 Å at 0.25 Å intervals. At each window, a harmonic biasing potential, $U(\delta\zeta) = k(\delta\zeta)^2$, was imposed by using an MMFP option in CHARMM. $\delta\zeta$ denotes the displacement from the center of the window, and k is the force constant that was set to 12 kcal·mol⁻¹·Å⁻² at all windows.

The cutoff distance for nonbonded interactions was set to 12 Å. For electrostatic interactions, the force switch method²² was used with a switching range of 8–12 Å. For van der Waals interactions, the shift method was used with the same switching range. The nonbond list was kept to 15 Å and updated heuristically. The MD time step size was 1 fs in all calculations.

At each window, the starting structure was energy minimized with the steepest descent method for 100 steps and then with the adopted basis Newton–Raphson method for 1000 steps. The system was heated in 50 K increments from 145.15 to 295.15 K for 5 ps at each temperature; 295.15 K (22 °C) was the experimental temperature condition.¹³ Following the heating runs, a 730 ps equilibration step was carried out by constant pressure and temperature simulations with the Hoover thermostat. During the equilibration run, the system slightly adjusted its volume to attain the proper density under 1 atm. The final production run was carried out at constant volume and temperature for 1 ns.

The Potential of Mean Force. The PMF was calculated by using the code distributed by A. Grossfield (<http://membrane.urmc.rochester.edu>), which implemented the weighted histogram analysis method (WHAM).²³ The value of ζ was sampled at every 100 fs, and the width of histogram bins was 0.05 Å.

The statistical error in the PMF was calculated by Monte Carlo bootstrap error analysis. At each window, 1000 synthetic data sets were generated randomly from the 1 ns production run trajectory. The trajectory was recorded at 0.1 ps time intervals, so that the actual data set contained 10 000 data points. However, for the bootstrap error analysis, one needs independent data points. The time required for the position autocorrelation function to decay to 1/e is about 1.65 ps (average value for all windows), and thus one may take the relaxation time of position autocorrelation to be about 3.3 ps. Taking this correlation time into account, each synthetic data set contained only 303 data points, ensuring on average about a 3.3 ps time interval between them. The standard deviations in $W(\zeta)$ calculated from the bootstrap error analysis were depicted as error bars in Figure 3. The average of the statistical errors for all windows was estimated to be ± 0.26 kcal·mol⁻¹.

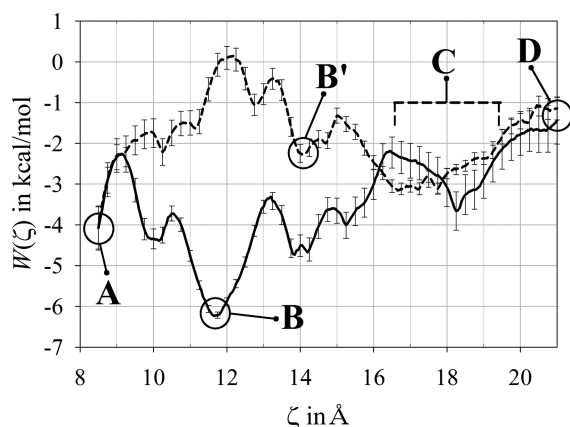


Figure 3. PMF as a function of the reaction coordinate ζ . The solid (dashed) curve represents the PMF when ATCh moves toward the active site with the choline (acetyl) part at the front side. The vertical bars represent the statistical errors.

In Figure 2, we also display the convergence behavior of the PMF profiles as the time length of MD trajectories increases. Although there remain small fluctuations in some places, the statistical errors do not affect much the estimates of the internal diffusion rate constants, k_2 and k'_2 .

Position-Dependent Diffusion Coefficient. It is assumed that the substrate motion along the reaction coordinate ζ may be described by the generalized Langevin equation. In addition, the natural potential is assumed to be locally flat in each window along ζ so that the main driving force comes from the harmonic biasing potential. These assumptions lead to

$$\mu \ddot{\zeta}(t) = -k\delta\zeta(t) - \int_0^t d\tau \chi(t-\tau) \dot{\zeta}(\tau) + R(t) \quad (3)$$

with the friction kernel χ and the random force R satisfying the fluctuation–dissipation relation, $\langle R(t)R(0) \rangle = k_B T \chi(t)$. The effective mass μ and the force constant k can be related respectively to the mean square velocity and the second moment of $\delta\zeta$ as $\mu = k_B T / \langle \dot{\zeta}^2 \rangle$ and $k = k_B T / \langle (\delta\zeta)^2 \rangle$.

In the overdamped limit, the diffusion coefficient in the window under consideration is given by the Einstein relation as

$$D = k_B T / \hat{\chi}(0) \quad (4)$$

where the caret symbol denotes a Laplace-transformed quantity: $\hat{f}(s) \equiv \int_0^\infty dt e^{-st} f(t)$. From eq 3, one can derive the relation between the friction kernel χ and the position autocorrelation function, $C_\zeta(t) \equiv \langle \delta\zeta(t) \delta\zeta(0) \rangle / \langle (\delta\zeta)^2 \rangle$, in the Laplace domain as $\hat{\chi}(s) = k[\hat{C}_\zeta(s)^{-1} - s]^{-1} - \mu s$. Hence, we have

$$D = \langle (\delta\zeta)^2 \rangle / \hat{C}_\zeta(0) \quad (5)$$

This relation was derived previously by Hummer in a slightly different way.²⁴

The Reaction Zone Configuration Integral. The rate constants k_{-1} and k'_{-1} in Scheme 1 are related to k_1 and k'_1 by

$$k_1/k_{-1} = V_{rx} \text{ and } k'_1/k'_{-1} = V'_{rx} \quad (6)$$

where V_{rx} and V'_{rx} are the configuration integrals over the spatial regions that define the E–S and E–S' states, respectively.²⁵ Here, we will describe the procedure for calculating V_{rx} ; V'_{rx} can be calculated in the same way.

V_{rx} is defined by

$$V_{rx} = \int_{rx} d\mathbf{R} e^{-\beta[W_R(\mathbf{R}) - W_R(|\mathbf{R}|=\infty)]} \quad (7)$$

where \mathbf{R} denotes the position vector of the CM of the substrate molecule relative to the CM of the enzyme, and $\int_{rx} d\mathbf{R}$ denotes the spatial integration over the reaction zone. $W_R(\mathbf{R})$ denotes the free energy defined as

$$\rho(\mathbf{R}') = \frac{\int d\mathbf{\Gamma} \delta(\mathbf{R}(\mathbf{\Gamma}) - \mathbf{R}') e^{-\beta V(\mathbf{\Gamma})}}{\int d\mathbf{\Gamma} e^{-\beta V(\mathbf{\Gamma})}} \propto e^{-\beta W_R(\mathbf{R}')} \quad (8)$$

Here, $\mathbf{\Gamma}$ denotes configurational coordinates for all atoms of the enzyme, substrate, and solvent molecules.

$W_R(\mathbf{R})$ may be represented as a sum of the contributions from long-range electrostatic interactions and short-range van der Waals interactions. Outside the enzyme, where the substrate molecule is surrounded by water molecules, the contributions to $W_R(\mathbf{R})$ and $W_R(|\mathbf{R}|=\infty)$ from the short-range van der Waals interactions will be canceled out. Hence, $[W_R(\mathbf{R}) - W_R(|\mathbf{R}|=\infty)] = V_E(\mathbf{R})$, where $V_E(\mathbf{R})$ denotes the potential energy of the substrate molecule in the electrostatic field of the enzyme. Hence, if we choose a reaction zone D such that the substrate molecule is fully surrounded by water molecules at least at the center of the reaction zone, one may make the following approximation:

$$\begin{aligned} V_{rx}^{(D)} &\cong \sum_i \Delta \mathbf{R}_i e^{-\beta[W_R(\mathbf{R}_i) - W_R(|\mathbf{R}|=\infty)]} \\ &= \Delta \mathbf{R}_c e^{-\beta[W_R(\mathbf{R}_c) - W_R(|\mathbf{R}|=\infty)]} \\ &\quad \times \sum_i (\Delta \mathbf{R}_i / \Delta \mathbf{R}_c) e^{-\beta[W_R(\mathbf{R}_i) - W_R(\mathbf{R}_c)]} \\ &\cong \Delta \mathbf{R}_c e^{-\beta V_E(\mathbf{R}_c)} \sum_i (\Delta \mathbf{R}_i / \Delta \mathbf{R}_c) [\rho(\mathbf{R}_i) / \rho(\mathbf{R}_c)] \end{aligned} \quad (9)$$

We have approximated the spatial integration in eq 7 as a sum of the contributions from small cells of volume $\Delta \mathbf{R}_i$ located at \mathbf{R}_i . In the second line, the subscript “c” denotes a cell located at the center of the reaction zone where the substrate molecule is fully surrounded by water molecules. If we have divided the reaction zone into equal size cells, we have

$$\begin{aligned} V_{rx}^{(D)} &\cong \Delta \mathbf{R}_c e^{-\beta V_E(\mathbf{R}_c)} \\ &\quad \times \left(\frac{\text{total residence time in the reaction zone}}{\text{residence time in the central cell}} \right) \end{aligned} \quad (10)$$

However, the reaction zone C that will be actually used to calculate the rate constant k_{-1} as well as k_2 is defined by a range of $\zeta \equiv |\mathbf{R}|$ with $\zeta_{\min}^{(C)} = 16.5 \text{ \AA}$ and $\zeta_{\max}^{(C)} = 19.5 \text{ \AA}$; see below. We can thus write

$$V_{rx}^{(C)} = \int_{\zeta_{\min}^{(C)}}^{\zeta_{\max}^{(C)}} d\zeta \zeta^2 \int d\mathbf{\Omega} e^{-\beta[W_R(\zeta, \mathbf{\Omega}) - W_R(|\mathbf{R}|=\infty)]} \quad (11)$$

Here, $\mathbf{\Omega}$ denotes the angular coordinates for \mathbf{R} . Since $\delta(\mathbf{R}(\mathbf{\Gamma}) - \mathbf{R}') = (\zeta')^{-2} \delta(\zeta(\mathbf{\Gamma}) - \zeta') \delta(\mathbf{\Omega}(\mathbf{\Gamma}) - \mathbf{\Omega}')$, we have

$$V_{rx}^{(C)} \propto \int_{\zeta_{\min}^{(C)}}^{\zeta_{\max}^{(C)}} d\zeta' e^{-\beta W(\zeta')} \quad (12)$$

where $W(\zeta)$ is the effective one-dimensional PMF that is calculated by the procedure described above; see Figure 3.

The above-mentioned reaction zone D may also be defined by a range of ζ values, if it is located near the active site channel entrance. We then have

$$V_{rx}^{(C)} = V_{rx}^{(D)} \times \frac{\int_{\zeta_{min}^{(C)}}^{\zeta_{max}^{(C)}} d\zeta' e^{-\beta W(\zeta')}}{\int_{\zeta_{min}^{(D)}}^{\zeta_{max}^{(D)}} d\zeta' e^{-\beta W(\zeta')}} \quad (13)$$

We chose the reaction zone D near the channel entrance with $\zeta_{min}^{(D)} = 20.5$ Å and $\zeta_{max}^{(D)} = 21.5$ Å. To calculate $V_{rx}^{(D)}$ by using eq 10, the central cell of reaction zone D was defined as a circular tube with the axis lying on the line connecting the CMs of the enzyme and ATCh molecule. Since the position of ATCh fluctuated, its position averaged over the 1 ns trajectory was used to define the central cell. The length of the tube was 1.0 Å ($= \zeta_{max}^{(D)} - \zeta_{min}^{(D)}$), and its radius was set to 1.0 Å, so that the volume of the central cell was approximately given by $\Delta R_c = \pi \text{ Å}^3$.

Electrostatic Potential Energy at the Active Site Channel Entrance. The electrostatic potential energy $V_E(\mathbf{R})$ of the substrate molecule around the enzyme was calculated by using the program DelPhi v.4,^{26,27} which solves the Poisson–Boltzmann equation numerically. For this calculation, we employed the Parse partial atomic charges and radii for the enzyme,²⁸ and the ATCh molecule was modeled as a dumbbell consisting of two overlapping spheres, representing the choline and the acetyl parts with charge of $+0.79e$ and $+0.21e$, respectively. The radii of both spheres were taken to be 2.8 Å, and the separation between the two was 4.63 Å. This dumbbell model of ATCh is that used in the previous BD simulation.⁹ With a grid spacing of 1.0 Å, the size of the solvent box was determined to be 137 Å, where the solute molecules filled 60% of the total volume. Internal and external dielectric constant values were 4 and 78,⁹ with the boundary defined by the solvent accessible surface of the enzyme and the ATCh molecule. Solvent and ionic probe radii were 1.4 and 2 Å, respectively. The boundary potentials were approximated by the Debye–Hückel potential of the equivalent dipole to the molecular charge distribution. The vacant space in the protein interior was filled with water molecules, and ions were excluded.

We calculated $V_E(\mathbf{R})$ at the mean position of the ATCh molecule averaged over a 1 ns trajectory. The ATCh molecule was placed along the channel axis, which was defined by the line connecting the CMs of the enzyme and ATCh molecule. The calculations were carried out for the two orientations of the ATCh dumbbell. In calculating $V_{rx}^{(D)}$ by using eq 10, the electrostatic potential at the central cell, $V_E(\mathbf{R}_c)$, was obtained by averaging the values at the five windows from $\zeta = 20$ Å to $\zeta = 21$ Å.

RESULTS AND DISCUSSION

The Rate Constants k_2 and k'_2 for the Internal Diffusion Step. From full-atom MD simulations with the explicit solvent model, the PMF has been calculated as a function of ζ by using WHAM.²³ The results are given in Figure 3. The solid (dashed) curve represents the PMF when ATCh moves toward the active site with the choline (acetyl) part at the front side. In the vicinity of the active site ($\zeta < 9$ Å), ATCh can reorient itself so that its orientation converges after a 750 ps equilibration step, regardless of the starting orientations. We can thus assume

that the solid and dashed curves match at $\zeta = 8.5$ Å. This matching results in the 0.29 kcal·mol^{−1} difference in energy between the two PMF curves at the opposite end (point D in Figure 3 at $\zeta = 21$ Å).

At point D, the ATCh molecule is not in close van der Waals contact with the enzyme. Hence, the energy difference between the two PMF curves at $\zeta = 21$ Å can be attributed mainly to the difference between electrostatic potential energies of the ATCh molecules with opposite orientations. By using DelPhi, we found that when the choline part of ATCh is at the front side toward the active site, the electrostatic potential energy is -1.3 kcal·mol^{−1} at a 179 mM ionic strength, while with the acetyl part at the front side it is -1.0 kcal·mol^{−1}. The estimated energy difference, 0.3 kcal·mol^{−1}, is in fair agreement with the PMF curves in Figure 3.

Figure 3 shows that the ATCh molecule confronts major potential energy barriers after the arrival at the potential minima (B for the solid curve and B' for the dashed curve). Figure 1A represents a snapshot at point B, while Figure 1B is that at point B'. In Figure 1A, the ATCh molecule is moving toward the active site (Ser203, red) with its choline part at the front side. The choline part has just passed over the bottleneck region between Tyr337 and Tyr124 (green), but the acetyl part is stuck in front of the bottleneck. In Figure 1B, the substrate molecule is heading for the active site with the acetyl part at the front side. The acetyl part has just arrived at the bottleneck region. Hence, the snapshots in Figure 1 and the PMF profiles in Figure 3 indicate that the acetyl part is more hindered than the choline part in passing through the bottleneck region of the channel. Since the size of the choline part is larger than the acetyl part, it is a counterintuitive finding. It seems that the hydrogen bonding between the carbonyl O of the acetyl part of ATCh and $-\text{OH}$ group of Tyr124 holds ATCh from going into the active site pocket.

In Figure 3, the shallow potential-well region C at the channel entrance ($16.5 \text{ Å} < \zeta < 19.5 \text{ Å}$) defines the E–S and E–S' states in Scheme 1. This region roughly corresponds to the reaction zone adopted by Antosiewicz et al.⁹ to calculate the rate constants k_1 and k'_1 for the external diffusion step.

The one-dimensional reaction coordinate model must be inappropriate inside the active site pocket since ATCh can also change its orientation. However, the PMF drops rather rapidly as ATCh enters the active site pocket. Therefore, we can equate the rate constant k_2 or k'_2 for the internal diffusion step to the inverse of MFPT from region C to point A at $\zeta = 8.5$ Å.

To check whether the calculated PMF, $W(\zeta)$, is free from a systematic bias depending on the chosen initial configuration at each window, we have carried out additional calculations as follows. At each window, after running the 1 ns trajectory, the center of harmonic biasing potential was moved inside by 0.25 Å, which is equal to the interval between sampling windows. In this way, the end point of the 1 ns trajectory of one window was chosen as the new initial system configuration for the neighboring window in the new set of calculations. After a 0.25 ns equilibration step for the system configuration to be relaxed in the new harmonic biasing potential with the displaced center, another 1 ns production run was carried out. The new PMF profiles obtained in this way are given in Figure S.1 in the Supporting Information. Their overall shapes are not much different from those given in Figure 3.

From MD simulations, the position-dependent diffusion coefficient of the substrate molecule along ζ has been calculated using eq 5. The diffusion coefficient fluctuates along the active

site channel (see Figure 4). The average value is $5.3 \text{ \AA}^2/\text{ns}$, which is about 15 times smaller than that in the bulk, $78 \text{ \AA}^2/\text{ns}$.⁹

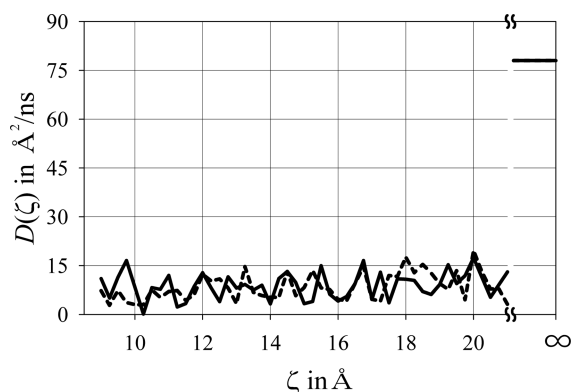


Figure 4. Variation of the diffusion coefficient of the substrate inside the active site channel. The solid (dashed) curve represents the value when ATCh moves toward the active site with the choline (acetyl) part at the front side. The horizontal line on the upper right corner represents the diffusion constant in the bulk, which is $78 \text{ \AA}^2/\text{ns}$.

The diffusion coefficient may also be calculated from the velocity autocorrelation function.^{29–31} The details of the calculation along this route are given in the Supporting Information. We obtained essentially the same result within the statistical errors.

With the PMF profile $W(\zeta)$ and the position-dependent diffusion coefficient $D(\zeta)$, we can calculate the MFPT from a point ζ_0 in region C to point A by

$$\tau(\zeta_0) = \int_{\zeta_0}^{\zeta_a} d\zeta' \frac{\exp[W(\zeta')/k_B T]}{D(\zeta')} \times \int_{\zeta_b}^{\zeta'} d\zeta'' \exp[-W(\zeta'')/k_B T] \quad (14)$$

ζ_a ($= 8.5 \text{ \AA}$) is the absorbing boundary (point A in Figure 3), and ζ_b ($= 19.5 \text{ \AA}$) is the reflecting boundary (the outer boundary of region C in Figure 3). For both PMF profiles in Figure 3, $\tau(\zeta_0)$ does not change much for $16.5 \text{ \AA} < \zeta_0 < 19.5 \text{ \AA}$; it varies from 170 to 172 ns for the solid curve and from 150 to 152 ns for the dashed curve. The rate constant for the internal diffusion step is then given by the inverse of the equilibrium average of $\tau(\zeta_0)$ over region C. k_2 and k'_2 calculated in this way are $5.8 (\pm 3.0) \times 10^6 \text{ s}^{-1}$ and $6.6 (\pm 2.6) \times 10^6 \text{ s}^{-1}$, respectively.

The Rate Constants k_{-1} and k'_{-1} . The rate constants k_{-1} and k'_{-1} in Scheme 1 can be estimated from eq 6. To calculate the reaction zone configuration integrals V_{rx} and V'_{rx} , we have to define the spatial regions corresponding to the E–S and E–S' states, respectively. These spatial regions are the reaction zones used to calculate k_1 and k'_1 . In our model, this reaction zone is the shallow potential-well region C at the channel entrance with $16.5 \text{ \AA} < \zeta < 19.5 \text{ \AA}$. It is slightly different from the reaction zone adopted by Antosiewicz et al.⁹ to calculate k_1 and k'_1 . However, if $k_{-1} \gg k_2$ and $k'_{-1} \gg k'_2$, we have

$$k_D = k_2 V_{rx} + k'_2 V'_{rx} \quad (15)$$

We will see shortly that this is the case for the present problem. For this internal diffusion-controlled case, the reaction zone model needs to be more consistent with the method of calculation of k_2 and k'_2 . The details of calculations of V_{rx} and V'_{rx} were described above. We have $V_{rx} = 7.8 \times 10^3 \text{ \AA}^3$ and $V'_{rx} = 1.0 \times 10^4 \text{ \AA}^3$, which give $k_{-1} = 2.2 \times 10^8 \text{ s}^{-1}$ and $k'_{-1} = 1.1 \times 10^8 \text{ s}^{-1}$,

respectively. As already mentioned, k_{-1} and k'_{-1} are orders of magnitude larger than k_2 and k'_2 .

The Overall Rate Constant k_D . From the results described above, eq 2 gives the overall rate constant as $k_D = 6.4(\pm 2.0) \times 10^7 \text{ M}^{-1} \text{ s}^{-1}$, while the approximate eq 15 gives $k_D = 6.7(\pm 2.1) \times 10^7 \text{ M}^{-1} \text{ s}^{-1}$, which are in good agreement with the experimental values of the apparent bimolecular rate constant, $k_{app} = 5.0 \times 10^7 \text{ M}^{-1} \text{ s}^{-1}$, quoted above. The statistical error in the calculated rate constant is rather large, but the experimental values for k_{app} are also quite scattered. For example, another reported value of k_{app} for the mouse AChE is $7.3 \times 10^7 \text{ M}^{-1} \text{ s}^{-1}$.³²

The fact that the difference between the estimates of k_D from eq 2 and eq 15 is negligible indicates that the substrate distribution is maintained at equilibrium up to the active site channel entrance, and the internal diffusion step is the rate-limiting one. Then, one may raise a question: why does k_{app} depend on the solvent viscosity? Obviously, the reaction zone configuration integrals, V_{rx} and V'_{rx} , do not. However, the internal diffusion rate constants, k_2 and k'_2 , will depend on the solvent viscosity in general.³³ In order for the ATCh molecule to pass through the bottleneck region of the channel between Tyr337 and Tyr124, large domains of the enzyme on which the two tyrosine residues are riding must move outward. The collective dynamics of large protein domains would depend on the solvent viscosity. If the external diffusion step were rate-limiting, k_D would be inversely proportional to the solvent viscosity. On the other hand, if the internal diffusion step is rate-limiting, k_D will show inverse fractional dependence on the solvent viscosity. Unfortunately, the available experimental data are insufficient to distinguish between these two possibilities.⁵

Effects of the Ionic Strength of Solution. The number of negatively charged residues of mAChE at pH 7.0, such as Asp and Glu, is larger than that of positively charged residues, such as Arg, so that the total charge of mAChE is $-8e$.¹⁴ It is known that the asymmetric charge distribution in AChE produces a very large dipole moment whose direction is oriented approximately along the axis of the active site channel. This dipole moment would steer the positively charged substrate or inhibitor approaching the enzyme to the entrance of the active site channel, resulting in the enhancement of the reaction rate.^{34,35} One may then expect that the enzyme reaction rate would depend to a great extent on the ionic strength of solution as well as on the mutation that disturb the asymmetric charge distribution.

Indeed, the reaction rate of AChE with the peripheral site ligands, such as fasciculin 2 (FAS2^{4+}) and *m*-trimethylammoniotrifluoroacetophenone (TFK^+), which are expected to inhibit enzyme reactivity by blocking the substrate to enter the active site channel, is enhanced considerably as the ionic strength gets lowered. However, the reaction rate of mAChE with ATCh (of +1 charge) does not change much with the ionic strength; the experimental values of k_{app} are $4.1 \times 10^7 \text{ M}^{-1} \text{ s}^{-1}$ (0 mM) and $2.5 \times 10^7 \text{ M}^{-1} \text{ s}^{-1}$ (670 mM).⁸

Equation 15 provides a quick estimate of the rate change with solvent ionic strength. Although the configuration integrals V_{rx} and V'_{rx} as well as the rate constants k_1 and k'_1 for the external diffusion of substrate from the bulk to the channel entrance, may increase considerably as the ionic strength decreases, the rate constants k_2 and k'_2 for the internal diffusion would not change much. Hence, assuming that the change in ionic strength affects only the electrostatic potential energy outside the enzyme, we may evaluate the ionic strength effect on k_D .

The electrostatic potential energy of ATCh at the channel entrance (point D at $\zeta = 21$ Å in Figure 3) has been calculated using DelPhi. When the choline part of ATCh is at the front side toward the active site, the electrostatic potential energies are -2.1 kcal·mol $^{-1}$, -1.3 kcal·mol $^{-1}$, and -1.1 kcal·mol $^{-1}$ at 0, 179, and 670 mM ionic strength, respectively. On the other hand, when the acetyl part is at the front side, they are -1.9 kcal·mol $^{-1}$, -1.0 kcal·mol $^{-1}$, and -0.80 kcal·mol $^{-1}$ at 0, 179, and 670 mM ionic strength, respectively.

Then from eq 15, the value of k_D at $I = 0$ mM, for example, may be estimated by

$$k_D(I = 0 \text{ mM}) = k_2 V_{rx}(I = 179 \text{ mM}) \times \exp[-(-2.1 + 1.3)/RT] + k'_2 V'_{rx}(I = 179 \text{ mM}) \times \exp[-(-1.9 + 1.0)/RT] \quad (16)$$

with $R = 1.987 \times 10^{-3}$ kcal K $^{-1}$ mol $^{-1}$. The values of k_D estimated in this way are 2.4×10^8 M $^{-1}$ s $^{-1}$ at $I = 0$ mM and 4.7×10^7 M $^{-1}$ s $^{-1}$ at $I = 670$ mM. We see that the estimate at the higher ionic strength solution with $I = 670$ mM is in fair agreement with the above quoted experimental value. However, the estimate at the zero ionic strength solution is about 6 times larger than the experimental value.

The reason for this large deviation of the theoretical estimate at low ionic strength can be attributed to the anomaly in the variation of experimental k_{app} values with ionic strength for the mAChE–ATCh reaction system.⁸ In contrast with the experimental results for AChE of other species, *T. californica* and human, the experimental value of k_{app} for mAChE does not increase monotonically as the ionic strength decreases; after going through a maximum value, it starts to decrease when the ionic strength gets close to zero [see Figures 2 and 8 of ref 8]. Indeed, the value of k_{app} at zero ionic strength is even lower than that at $I = 179$ mM. It may be possible that the rate constants k_2 and k'_2 decrease as the ionic strength becomes very low, because the positively charged substrate molecule may be held longer at the active site channel entrance due to the bare electrostatic attraction by nearby negatively charged residues. A further investigation on the changes in k_2 and k'_2 , as well as the possible change in the mAChE structure, at low ionic strength based on more extensive MD simulations would be required.

Effects of the Enzyme Mutation. Reaction rates of point-mutated AChE enzymes were investigated experimentally,^{8,13} and also by BD simulations with the assumption that the change in protein conformation due to the mutation was not big.¹⁰ It was found that the extent of decrease in the rate due to neutralization mutation of a negatively charged residue is moderate when the mutated residue is located at the enzyme surface; the reaction rates of the mutant enzymes are 2 or 3 times lower than that of the wild type.³⁶ In contrast, the neutralization mutation of a residue inside the active site channel gives rise to an order of magnitude decrease in the rate.

It seems that the mutation of the inside residue changes the rate constants k_2 and k'_2 for the rate-determining internal diffusion step; evaluation of such mutation effects would require extensive MD simulations. However, the rate change due to neutralization mutation of the negatively charged residues on the enzyme surface may be estimated quickly from eq 15. For simplicity, we will assume that the mutation of surface residues

modifies the electrostatic potential contribution to the configuration integrals V_{rx} and V'_{rx} but does not change the internal diffusion rate much.

The values of V_{rx} and V'_{rx} for the native mAChE are larger than those for the mutants owing to the attractive electrostatic interaction between ATCh and the negatively charged residue, which will be denoted as $E_{\text{ATCh-residue}}$ or $E'_{\text{ATCh-residue}}$ depending on the orientation of ATCh. With the assumption that the change in protein conformation due to the mutation is not big, we make the following approximation:

$$\frac{V_{rx}(\text{wild type})}{V_{rx}(\text{mutant})} \cong \exp\left[-\frac{E_{\text{ATCh-residue}}}{k_B T}\right] \quad (17)$$

The ratio $V'_{rx}(\text{wild type})/V'_{rx}(\text{mutant})$ is determined similarly with $E'_{\text{ATCh-residue}}$. In calculating $E_{\text{ATCh-residue}}$ and $E'_{\text{ATCh-residue}}$, the ATCh molecule has been modeled as a dumbbell with two point charges and the negatively charged residue of interest as a set of charges given by the CHARMM parameter set 22.¹⁷ Because the space between the residue and the ATCh molecule at the active site channel entrance is filled with both the protein medium and the solvent, a distance-dependent dielectric model with $\epsilon_r = 2r$ has been used to calculate $E_{\text{ATCh-residue}}$ and $E'_{\text{ATCh-residue}}$.³⁷

The calculated results for the mutation effects are presented in Table 1. In spite of the rough approximations, our estimates are in reasonable agreement with the experimental data,⁸ except the case of D283N and E292Q.

In the case of D283N and E292Q, the mutated residues Asp283 and Glu292 are located closer to the active site channel entrance. It seems that these negatively charged residues also affect the internal diffusion of ATCh (k_2 and k'_2). In the native enzyme, these negatively charged residues at the channel entrance attract the ATCh molecule more effectively and enhance the rate of external diffusion from the bulk to the channel entrance. But it may be possible that they hold the ATCh molecule around them, and thus they retard the internal diffusion of ATCh toward the active site. In estimating the mutation effects listed in Table 1, we have taken into account only the effects on the

Table 1. Rate Constants for the Reaction of ATCh with Mutant Enzymes^a

	distance	$E_{\text{ATCh-residue}}$	$E'_{\text{ATCh-residue}}$	calculation	experiment
wild type				6.7	5.0
E84Q	19.6	−0.42	−0.38	3.2	2.5
E91Q	24.3	−0.27	−0.25	4.0	3.7
D280V	18.4	−0.46	−0.49	2.8	2.7
D283N	13.7	−0.90	−0.95	1.3	3.5
E292Q	9.31	−1.2	−1.5	0.69	3.2
D372N	25.1	−0.30	−0.32	3.8	3.2
E84Q/E91Q		−0.70	−0.63	2.1	1.5

^aThe second column lists the distance (in Å) between the carboxyl carbon of the mutated residue and ATCh (the dumbbell center). $E_{\text{ATCh-residue}}$ and $E'_{\text{ATCh-residue}}$ are in kcal·mol $^{-1}$, and the rates are in 10^7 M $^{-1}$ s $^{-1}$. The calculation is based on eq 15, so that the listed value of k_D for the wild type enzyme is that obtained from eq 15.

external diffusion. The neutralization mutation of Asp283 or Glu292 would reduce the rate of external diffusive approach of ATCh as estimated above, but it may enhance the internal diffusion rate toward the active site. Further studies on the kinetics of mutant enzymes like D283N and E292Q are in progress based

on more extensive MD simulations of the internal diffusion step.

CONCLUSION

Previous computational studies provided reasonable accounts of the various aspects of the acetylcholinesterase kinetics, such as the relative changes in the reaction rate due to the variation of solvent ionic strength and the mutation of negatively charged surface residues and so on. However, as for the absolute value of the rate constant, any satisfactory account has been absent.^{9–11,38,39}

With the foresight that the internal diffusion of substrate inside the active site channel can limit the reaction rate, we have calculated the transit time for the substrate molecule to reach the active site starting from the channel entrance based on full-atom MD simulations. Bui et al.¹² carried out a similar calculation, but they only considered the bulkier choline part, excluding the acetyl part of the substrate in the simulation. However, as we have seen from Figures 1 and 3, it is crucial to include the acetyl part in determining the major potential barrier. From the MD simulations, we have calculated the PMF profile and the position-dependent diffusion coefficient for the effective one-dimensional motion of the substrate molecule inside the channel and thereby determined the mean first passage time of the substrate from the channel entrance to the active site.

The calculation shows that the internal substrate diffusion is the determinant of the acetylcholinesterase kinetics in the low substrate concentration limit, at least for the mAChE–ATCh reaction system. The estimate for the internal diffusion rate combined with the reaction zone configurational integral provides a quantitative estimate of the overall bimolecular rate constant in good agreement with the experimental data. In addition, the present calculation provides a quick and reasonable explanation for the effects of the solvent ionic strength and the mutation of surface residues of the enzyme, although more extensive calculations based on full-atom MD simulations are necessary to get quantitative results.

ASSOCIATED CONTENT

Supporting Information

The PMF $W(\zeta)$ calculated from the new set of 1 ns trajectories obtained after the center of harmonic biasing potential was moved inside by 0.25 Å at each window and the position-dependent diffusion coefficient $D(\zeta)$ calculated from the velocity autocorrelation function. This information is available free of charge via the Internet at <http://pubs.acs.org>

AUTHOR INFORMATION

Corresponding Author

*E-mail: sangyoub@snu.ac.kr.

Notes

The authors declare no competing financial interest.

ACKNOWLEDGMENTS

This work was supported by the National Research Foundation (NRF) grants (No. 2009-0074693 and No. 2010-0001631) funded by the Korean government (MEST).

REFERENCES

(1) Doctor, B. P. *Structure and Function of Cholinesterase and Related Proteins*; Plenum Press: New York, 1998.

- (2) Soreq, H.; Seidman, S. *Nat. Rev. Neurosci.* **2001**, *2*, 294–302.
- (3) Shen, T.; Tai, K.; Henschman, R. H.; McCammon, J. A. *Acc. Chem. Res.* **2002**, *35*, 332–340.
- (4) Ellman, G. L.; Courtney, K. D.; Andres, V. Jr.; Featherstone, R. M. *Biochem. Pharmacol.* **1961**, *7*, 88–95.
- (5) Bazelyansky, M.; Robey, E.; Kirsch, J. F. *Biochemistry* **1986**, *25*, 125–130.
- (6) Berman, H. A.; Leonard, K. *Biochemistry* **1990**, *29*, 10640–10649.
- (7) Radic, Z.; Gibney, G.; Kawamoto, S.; MacPhee-Quigley, K.; Bongiorno, C.; Taylor, P. *Biochemistry* **1992**, *31*, 9760–9767.
- (8) Radic, Z.; Kirchhoff, P. D.; Quinn, D. M.; McCammon, J. A.; Taylor, P. *J. Biol. Chem.* **1997**, *272*, 23265–23277.
- (9) Antosiewicz, J.; Gilson, M. K.; Lee, I. H.; McCammon, J. A. *Biophys. J.* **1995**, *68*, 62–68.
- (10) Antosiewicz, J.; McCammon, J. A.; Wlodek, S. T.; Gilson, M. K. *Biochemistry* **1995**, *34*, 4211–4219.
- (11) Zhou, H.; Briggs, J. M.; McCammon, J. A. *J. Am. Chem. Soc.* **1996**, *118*, 13069–13070.
- (12) Bui, J. M.; Henschman, R. H.; McCammon, J. A. *Biophys. J.* **2003**, *85*, 2267–2272.
- (13) Radic, Z.; Pickering, N. A.; Vellom, D. C.; Camp, S.; Taylor, P. *Biochemistry* **1993**, *32*, 12074–12084.
- (14) Felder, C. E.; Botti, S. A.; Lifson, S.; Silman, I.; Sussman, J. L. *J. Mol. Graphics Model.* **1997**, *15*, 318–327.
- (15) Szabo, A.; Schulten, K.; Schulten, Z. *J. Chem. Phys.* **1980**, *72*, 4350–4357.
- (16) Brooks, B. R.; Bruccoleri, R. E.; Olafson, B. D.; States, D. J.; Swaminathan, S.; Karplus, M. *J. Comput. Chem.* **1983**, *4*, 187–217.
- (17) MacKerell, A. D. Jr.; Bashford, D.; Bellott, M.; Dunbrack, R. L. Jr.; Evanseck, J. D.; Field, M. J.; Fischer, S.; Gao, J.; Guo, H.; Ha, S.; Joseph-McCarthy, D.; Kuchnir, L.; Kucsera, K.; Lau, F. T. K.; Mattos, C.; Michnick, S.; Ngo, T.; Nguyen, D. T.; Prodhom, B.; Reiher, W. E. III; Roux, B.; Schlenkrich, M.; Smith, J. C.; Stote, R.; Straub, J.; Watanabe, M.; Wiorkiewicz-Kuczera, J.; Yin, D.; Karplus, M. *J. Phys. Chem. B* **1998**, *102*, 3586–3616.
- (18) Bourne, Y.; Taylor, P.; Radic, Z.; Marchot, P. *EMBO J.* **2003**, *22*, 1–22.
- (19) Brunger, A. T.; Karplus, M. *Proteins: Struct., Funct., Genet.* **1988**, *4*, 148–156.
- (20) Schmidt, M. W.; Baldridge, K. K.; Boatz, J. A.; Elbert, S. T.; Gordon, M. S.; Jensen, J. H.; Koseki, S.; Matsunaga, N.; Nguyen, K. A.; Su, S.; Windus, T. L.; Dupuis, M.; Montgomery, J. A. Jr. *J. Comput. Chem.* **1993**, *14*, 1347–1363.
- (21) Raves, M. L.; Harel, M.; Pang, Y. -P.; Silman, I.; Kozikowski, A. P.; Sussman, J. L. *Nat. Struct. Biol.* **1997**, *4*, 57–63.
- (22) Steinbach, P. J.; Brooks, B. R. *J. Comput. Chem.* **1994**, *15*, 667–683.
- (23) Kumar, S.; Bouzida, D.; Swendsen, R. H.; Kollman, P. A.; Rosenberg, J. M. *J. Comput. Chem.* **1992**, *13*, 1011–1021.
- (24) Hummer, G. *New J. Phys.* **2005**, *34*.
- (25) Lee, S.; Karplus, M. *J. Chem. Phys.* **1987**, *86*, 1883–1903; *Erratum, ibid* **1992**, *96*, 1663.
- (26) Rocchia, W.; Alexov, E.; Honig, B. *J. Phys. Chem. B* **2001**, *105*, 6507–6514.
- (27) Rocchia, W.; Sridharan, S.; Nicholls, A.; Alexov, E.; Chiabrera, A.; Honig, B. *J. Comput. Chem.* **2002**, *23*, 128–137.
- (28) Sitkoff, D.; Sharp, K. A.; Honig, B. *J. Phys. Chem.* **1994**, *98*, 1978–1988.
- (29) Crouzy, S.; Woolf, T. B.; Roux, B. *Biophys. J.* **1994**, *67*, 1370–1386.
- (30) Schumaker, M. F.; Pomes, R.; Roux, B. *Biophys. J.* **2000**, *79*, 2840–2857.
- (31) Mamonov, A. B.; Kurnikova, M. G.; Coalson, R. D. *Biophys. Chem.* **2006**, *124*, 268–278.
- (32) Vellom, D. C.; Radic, Z.; Li, Y.; Pickering, N. A.; Camp, S.; Taylor, P. *Biochemistry* **1993**, *32*, 12–17.
- (33) Doster, W. *Biophys. Chem.* **1983**, *17*, 97–103.
- (34) Tan, R. C.; Truong, T. N.; McCammon, J. A.; Sussman, J. L. *Biochemistry* **1993**, *32*, 401–403.

- (35) Ripoll, D. R.; Faerman, C. H.; Axelsen, P. H.; Silman, I.; Sussman, J. L. *Proc. Natl. Acad. Sci. U. S. A.* **1993**, *90*, 5128–5132.
- (36) Shafferman, A.; Ordentlich, A.; Barak, D.; Kronman, C.; Ber, R.; Bino, T.; Ariel, N.; Osman, R.; Velan, B. *EMBO J.* **1994**, *13*, 3448–3455.
- (37) Murray, J. S.; Sen, K. D. *Molecular Electrostatic Potentials: Concepts and Applications*; Elsevier: Amsterdam, 1996.
- (38) Antosiewicz, J.; Wlodek, S. T.; McCammon, J. A. *Biopolymer* **1996**, *39*, 85–94.
- (39) Zhou, H.; Wlodek, S. T.; McCammon, J. A. *Proc. Natl. Acad. Sci. U. S. A.* **1998**, *95*, 9280–9283.